Quantum walks and quantum search on graphene lattices

Iain Foulger, Sven Gnutzmann, and Gregor Tanner
School of Mathematical Sciences, University of Nottingham, University Park, Nottingham NG7 2RD, UK.

Quantum walks have been very useful in developing search algorithms in quantum information, in particular for devising of spatial search algorithms. However, the construction of continuous-time quantum search algorithms in two-dimensional lattices has proved difficult, requiring additional degrees of freedom. Here, we demonstrate that continuous-time quantum walk search is possible in two-dimensions by changing the search topology to a graphene lattice, utilising the Dirac point in the energy spectrum. This is made possible by making a change to standard methods of marking a particular site in the lattice. Various ways of marking a site are shown to result in successful search protocols. We further establish that the search can be adapted to transfer probability amplitude across the lattice between specific lattice sites thus establishing a line of communication between these sites.

PACS numbers: 03.67.Hk, 72.80.Vp, 03.65.Sq, 03.67.Lx

arXiv:1501.07543v2 [quant-ph] 1 Jul 2015

I. INTRODUCTION

Quantum walks have been a particularly fruitful field of research in quantum information going back to ideas from Feynman [1], Meyer [2], and Aharonov [3]. One focus of recent work on quantum walks is their application to spatial search algorithms. It is well-known that Grover's algorithm [4, 5] for searching on unstructured databases offers a quadratic improvement in search time over classical models. Grover's algorithm is not designed to search physical systems where only local operations are possible and quantum walk algorithms have been employed for this purpose. In developing such algorithms, the major consideration is the search time attempting to match the quadratic improvement over the classical case offered by Grover's algorithm. The first spatial search algorithm to do this, using the standard model of quantum walks, was developed by Shenvi, Kempe and Whaley [6] for searches on a hypercube.

While there exist discrete-time searches on d-dimensional cubic lattices which are faster than classical searches for $d \geq 2$ [7] , effective continuous-time quantum searches only exist for $d \geq 4$ [8] or else they require additional memory (in the form of spin degrees of freedom) in order to improve their search time in lower dimensions [9]. In [10], we demonstrated that effective searches over two-dimensional lattices may be achieved in an arguably simpler way which does not require extra degrees of freedom, and could, therefore, be viewed as more efficient. This is achieved through the choice of a different lattice, specifically, a honeycomb lattice which is the underlying lattice structure of carbon atoms in the material graphene.

The association with graphene is important as, although we first study a purely theoretical problem in quantum information, the use of a graphene lattice also offers a potential physical realisation. We thus envisage using the quantum walk and quantum search algorithm framework to investigate the effect of perturbations on the dynamics on graphene and other carbon structures. This offers not only the possibility for demonstrating two-dimensional continuous-time quantum searching, but also paves the way for looking for novel effects in the material graphene.

In this paper, we offer a detailed account of the theory and numerical results thus expanding on the findings as presented in [10]. Generalisations of the results in [10] have been given in [11], where a approach to solving the problem has been taken through encoding extra degrees of freedom into crystal lattices. Recent experiments on artificial microwave graphene [12] have shown that additional site perturbations, as discussed in Sec. VII, can be used to create a search protocol. Searching on honeycomb lattices in discrete-time setting has been considered in [13]; however, no improvement over discrete time searches on cubic lattices was found.

The paper is structured as follows: In Section II we give an introduction to the formalism of continuous-time quantum walks and the construction of quantum walk search algorithms. We also explain why previous search algorithms struggled on lower-dimensional lattices and why graphene offers a solution. Section III will detail the relevant properties of graphene and set-up the notation we shall use throughout. Sections IV & V contain our main analytical results, where we detail the specifics of our search algorithm and offer an analysis of the search running time and success probability. We shall then show in Section VI how this search protocol can be adapted to demonstrate novel communication setups. Sections VII & VIII contain numerical work demonstrating the possibility of using alternative methods of marking to create search behaviour and other carbon nanostructures. We conclude with a review and discussion of our results in Section IX.

II. QUANTUM WALKS AND SEARCHING

Continuous-time quantum walks (CTQW), first defined in [14], are the quantum analogue of continuous-time Markov chains. They are defined purely on the state space, that is, the Hilbert space $\mathcal{H}_p$, spanned by

the states $|j\rangle$ which represent the j^{th} site of the lattice. Thus, the time-evolution of such systems is defined by the Schödinger equation

$$\frac{d}{dt}\alpha_j(t) = -i\sum_{l=1}^{N}\mathbf{H}_{jl}\alpha_l(t)\ , \tag{1}$$

where $\alpha_j = \langle j|\,\psi(t)\,\rangle$ is the probability amplitude at the j^{th} vertex of a system described by the state vector $|\psi(t)\rangle$, and $\mathbf{H}$ is the Hamiltonian describing the connectivity of the lattice. Note that we are using a dimensionless description setting e.g. $\hbar = 1$.

The dynamics of a quantum walk over a network is defined by the nature of the interaction between connected sites. Therefore, the Hamiltonian is generally constructed from the adjacency matrix of the underlying lattice. The adjacency matrix $\mathbf{A}$ is defined as

$$\mathbf{A}_{jl} = \begin{cases} 1 & \text{if } j \text{ and } l \text{ are connected} \\ 0 & \text{if } j \text{ and } l \text{ are not connected.} \end{cases} \tag{2}$$

Typically, the Hamiltonian is chosen as $\mathbf{H} = \epsilon_D\mathbf{I} + v\mathbf{A}$. The parameter v determines the coupling strength between connected sites and the parameter ϵ_D is an on-site energy that only enters the dynamics in a trivial way and thus can be set to a desired value. If $v = -1$ and ϵ_D is equal to the valency of the lattice $\mathbf{H}$ is the discrete Laplacian. This form of Hamiltonian is closely related to the tight-binding model for condensed matter systems [15].

As first explained in [16, 17], a quantum walk is transformed into a search protocol by introducing a localised perturber state, forming an avoided crossing in the spectrum of the search Hamiltonian between an unperturbed eigenstate and the localised perturber. Thus, initialising the system in the unperturbed eigenstate involved in the crossing and allowing the system to evolve in time, one finds that the system rotates into the localised perturber state.

The first CTQW search over d-dimensional cubic lattices [8] introduced the localised perturber state as a projector onto a single site w, resulting in the search Hamiltonian

$$\mathbf{H}_\gamma = -\gamma\mathbf{A} + |w\rangle\langle w|\ . \tag{3}$$

Here, γ is a parameter governing the strength of interactions between sites in the lattice. This parameter is chosen carefully [8] such that the perturber state $|w\rangle$ is brought into resonance with the ground state of the unperturbed Hamiltonian, the uniform superposition $|s\rangle$.

Let us assume for the moment that all other unperturbed eigenstates are energetically sufficiently separated from the ground state – we will come back to this assumption later. Then there will be an avoided crossing of two eigenvalues corresponding to the perturber state and the ground state. Perturbation theory estimates that the energy splitting of these resonant states is proportional to the overlap of the localised perturber state $|w\rangle$ and the uniform ground state $|s\rangle$, which scales as

$$\Delta E \sim |\langle w|s\rangle| \sim N^{-1/2}\,, \tag{4}$$

and that the corresponding eigenstates are of the form $(|s\rangle \pm |w\rangle)/\sqrt{2}$. By preparing the system initially in $|s\rangle$ and allowing it to evolve for a set period of time $T = \pi/\Delta E \propto \sqrt{N}$, a measurement of the system will result in the state $|w\rangle$ being measured with high probability. This explains the speed-up of the quantum walk search. The Grover algorithm and its speed-up can be understood in analogous terms and one can show that all other states are indeed energetically very well separated.

In the present case this separation only holds above a critical dimension $d_c = 4$. A simple argument for the critical dimension can be obtained by comparing the scaling behaviour of the energy splitting $\Delta E \sim N^{-1/2}$ with the energy separation of the first excited state from the ground state in the unperturbed lattice. For a cubic lattice we have a quadratic dispersion relation which allows us to estimate the energy separation

$$E(\underline{k}) - E_0 \sim |\underline{k}|^2 \sim N^{-2/d}$$

(as $|\underline{k}| \sim N^{-1/d}$ for the first excited state in a d-dimensional lattice). For $d > 4$ one then has $\Delta E/(E(\underline{k}) - E_0) \to 0$ as $N \to \infty$ and a detailed analysis indeed proves that the quantum walk search works with optimal speed-up [8]. At the critical dimension $d = 4$ the two energy scales scale in the same way – the detailed analysis shows that the search still works but the dynamics is more complicated due to the interference of excited states. While there is still a speed-up it is only almost optimal; the optimal search time $T \propto N^{1/2}$ gets multiplied with a logarithmically increasing factor. For the experimentally relevant regimes of 2- and 3-dimensional cubic lattices, all states participate in the dynamics as any avoided crossing gets dissolved completely as the number of sites grows. As a result no speed-up over classical searches is found.

The above estimate offers a simple way how to reduce the critical dimension. If one can construct a search around a uniformly distributed state at an energy E_0 where the dispersion relation is conic (linear in $|\underline{k}|$), then in d dimensions

$$E - E_0 \sim |\underline{k}| \sim N^{1/d}$$

which results in a critical dimension $d_c = 2$. In [9] this was implemented using a modified Dirac Hamiltonian. However, this requires the addition of a spin degree of freedom, essentially a doubling of memory, with the added complication that it is not immediately clear how such a system would be physically realised.

Instead, our solution here is to change the lattice from a square (cubic) to a graphene lattice. This change of topology automatically implies the first step in our solution, as one of the important electronic features of graphene is the conic dispersion relation around the Dirac energy. This arises naturally from the tight-binding descriptions of graphene. Note that graphene has the critical dimension $d = 2$. Indeed our construction as presented in [10] has an almost optimal speed-up with logarithmic corrections that need to be evaluated in a de-

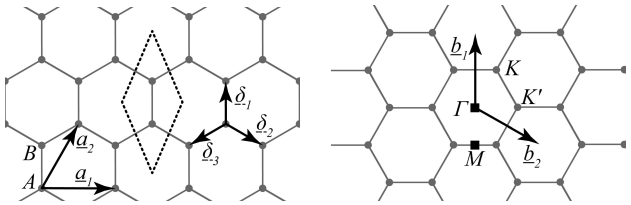


FIG. 1. Left: Graphene with lattice vectors $\underline{a}_{1/2}$, translation vectors $\underline{\delta}_i$ and unit cell (dashed lines). Right: Reciprocal lattice with basis vectors $\underline{b}_{1/2}$, symmetry points $\underline{\Gamma}$, $\underline{K}$, $\underline{K}'$, $\underline{M}$ and first Brillouin zone (hexagon).

tailed analysis that goes beyond the simple perturbative description given above.

III. RELEVANT PROPERTIES OF GRAPHENE

Graphene is a single layer of carbon atoms arranged in a honeycomb lattice. The lattice is bipartite with two sublattices, labelled A and B, and a unit cell containing two carbon atoms. The spatial and reciprocal lattices are shown in Figure 1. The primitive vectors describing the lattice are $\underline{a}_{1(2)}$, such that the position of a unit cell in the lattice is given by $\underline{R}(\alpha,\beta) = \alpha a_1 + \beta a_2$. We use dimensionless units in space where the distance between nearest neighbor sites is $a = 1$. The reciprocal lattice shows two important points, the Dirac points $\underline{K}$ and $\underline{K}'$ at the two inequivalent corners of the Brillouin zone.

The energy spectrum of electrons in graphene was first derived by Wallace [18] when considering the band structure of graphite using a tight-binding Hamiltonian

$$\mathbf{H} = \epsilon_D \mathbf{1} + v\mathbf{A} \tag{5}$$

where ϵ_D is the on-site energy (which we will identify as the energy of the Dirac points) and v the hopping strength (both dimensionless in our setting). The tight-binding model for graphene and the derivation of the solution are well-known [19, 20] and give rise to the dispersion relation

$$\epsilon(\underline{k}) = \epsilon_D \pm v\sqrt{1 + 4\cos^2\left(\frac{k_x}{2}\right) + 4\cos\left(\frac{k_x}{2}\right)\cos\left(\frac{\sqrt{3}k_y}{2}\right)}, \tag{6}$$

shown in Figure 2 for an infinite graphene lattice.

As there are two atoms per unit cell the spectrum has two branches, the upper branch being the conduction band and the lower the valence band, which meet at the corners of the Brillouin zone, the $\underline{K}$-points. The energy at the $\underline{K}$-points is ϵ_D which we name the Dirac energy. It is around these points, that the behaviour of the spectrum is conical, that is,

$$\epsilon(\underline{k}) \approx \epsilon_D \pm v\frac{\sqrt{3}}{2}\sqrt{\delta k_x^2 + \delta k_y^2} = \epsilon_D \pm v\frac{\sqrt{3}}{2}|\delta k|, \tag{7}$$

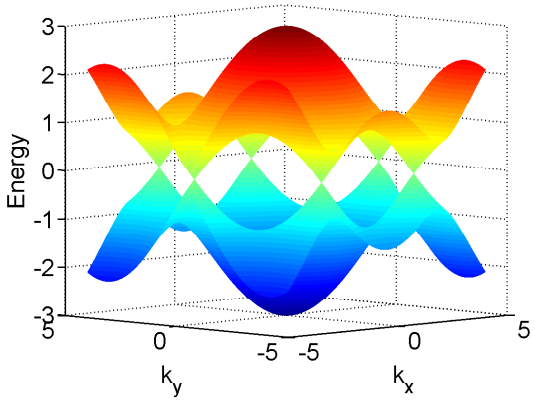


FIG. 2. (Color online) Dispersion relation for infinite graphene sheet ($\epsilon_D = 0$ and $v = -1$).

with a reduced density of states, a necessary feature for the creation of the search dynamics.

As the lattice possesses a translational symmetry the Hamiltonian can be solved using linear superpositions of Bloch functions over both sublattices. As a basis we use the orthonormal states $\{|\alpha,\beta\rangle^A, |\alpha,\beta\rangle^B\}$ to denote states on either the A or B sublattice in the cell at position $\underline{R}(\alpha,\beta)$. For the majority of what follows (except in Section VIII), we will focus on finite-sized lattices with assumed periodic boundary conditions along the axes of both primitive vectors so that the topology of our lattice is a torus; that is, our wavefunction is of the general form $|\psi\rangle = \sum_{\alpha=1}^{m}\sum_{\beta=1}^{n}\left(\psi^A_{\alpha,\beta}|\alpha,\beta\rangle^A + \psi^B_{\alpha,\beta}|\alpha,\beta\rangle^B\right)$. Our boundary conditions imply that the state vector must satisfy $\psi^{A(B)}_{\alpha,\beta} = \psi^{A(B)}_{\alpha+m,\beta} = \psi^{A(B)}_{\alpha,\beta+n}$ where m, n denote the period of the lattice. Thus, the wavefunctions on the torus take the Bloch function form

$$|\psi\rangle = \sum_{(\alpha,\beta)}\left[\frac{1}{\sqrt{N}}e^{i\underline{k}\cdot\underline{R}(\alpha,\beta)}|\alpha,\beta\rangle^A + \frac{C(\underline{k})}{\sqrt{N}}e^{i\underline{k}\cdot(\underline{R}(\alpha,\beta)+\underline{\delta}_1)}|\alpha,\beta\rangle^B\right], \tag{8}$$

where N is the number of sites in the lattice, $\underline{k}$ is the momentum, and $C(\underline{k})$ is a relative phase contribution dependent upon whether the state belongs to the conduction or valence bands; it can be calculated by explicitly working through the tight-binding model.

Application of the periodic boundary conditions results in the following quantised momenta

$$k_x = \frac{2\pi p}{m}, \qquad k_y = \frac{1}{\sqrt{3}}\left(\frac{4\pi q}{n} - k_x\right), \tag{9}$$

where $p \in \{0, 1, \ldots m-1\}$ and $q \in \{0, 1, \ldots n-1\}$. In the following and whenever we consider quantum walk dynamics on a torus, the number of cells in each direction is generally chosen to be the same, that is, $m = n = \sqrt{\frac{N}{2}}$. This choice is purely for simplifying the notation; alternative torus dimensions are possible as are other choices

of boundary conditions corresponding to alternative carbon structures (e.g. nanotubes or a graphene sheet) as will be demonstrated in Section VIII. For our choice of torus dimensions, we find there are momenta equal to the $\underline{K}$-points and, consequently, eigenstates with energies equal to the Dirac energy when both m and n are some multiple of 3.

In fact, using the quantised momenta in Eq. (9) obtained for periodic boundary conditions, we find that there are four degenerate eigenstates with an energy that coincides exactly with the Dirac energy when m and n are both multiples of 3. These four states, known as the Dirac states, can be constructed to live only on one of the sublattices, and are given by

$$\begin{aligned} \left|\underline{K}\right\rangle^{A(B)} &= \sqrt{\frac{2}{N}} \sum_{(\alpha,\beta)} e^{i\frac{2\pi}{3}(\alpha+2\beta+2\sigma)} \left|\alpha,\beta\right\rangle^{A(B)} \\ \left|\underline{K}'\right\rangle^{A(B)} &= \sqrt{\frac{2}{N}} \sum_{(\alpha,\beta)} e^{i\frac{2\pi}{3}(2\alpha+\beta)} \left|\alpha,\beta\right\rangle^{A(B)} , \end{aligned} \tag{10}$$

where $\sigma = 0$ for states on the A-sublattice or $\sigma = 1$ for states on the B-sublattice.

IV. QUANTUM SEARCH ON GRAPHENE - REDUCED MODEL

In this section we will describe how a site is marked and will derive our optimal search starting state. Our approach will be to analyse the system's spectrum and its dynamics in a reduced Hamiltonian model involving only the relevant states from the avoided crossing. In the next section we will then validate this approach with a more detailed analysis, using the results obtained here as an initial guide.

As already established, we introduce the localised perturber state in a region of the spectrum with a conic dispersion relation and thus a low density of states. Simply altering the on-site energy in Eq. (3) as done in [8] does, however, not work here. As the on-site energy ϵ_D and the Dirac energy are equal, one finds that the perturbation only interacts with the Dirac states in the limit of zero perturbation strength, returning the unperturbed lattice. Therefore, we choose an alternative perturbation method: namely, we modify the coupling strength between the site we wish to mark and its neighboring vertices. We focus in this section on changing the coupling to all three neighboring vertices of a particular site equally. Our choice of perturbation matrix $\mathbf{W}$ to mark the A-type vertex $(\alpha_o,\beta_o)^A$ is then

$$\mathbf{W} = \sqrt{3}\left|\ell\right\rangle\left\langle\alpha_o,\beta_o\right|^A + \sqrt{3}\left|\alpha_o,\beta_o\right\rangle^A\left\langle\ell\right| , \tag{11}$$

where the state $|\ell\rangle$ is the symmetric superposition over the three neighbors of the perturbed site

$$\left|\ell\right\rangle = \frac{1}{\sqrt{3}}\left(\left|\alpha_o-1,\beta_o\right\rangle^B + \left|\alpha_o-1,\beta_o+1\right\rangle^B + \left|\alpha_o,\beta_o\right\rangle^B\right) . \tag{12}$$

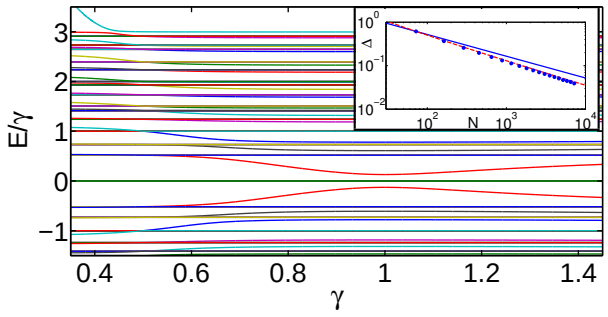


FIG. 3. (Color online) Spectrum of $\mathbf{H}_\gamma$ in Equation (13) as a function of γ for a 12×12 cell torus ($N = 288$). The spectrum is symmetric around $\epsilon_D = 0$. Inset: Scaling of the gap $\Delta = \tilde{E}_+ - \tilde{E}_-$ (dots) and curves $c_1/\sqrt{N}$ (solid blue), $c_2/\sqrt{N\log N}$ (dashed red) for comparison.

This leaves us with the search Hamiltonian

$$\mathbf{H}_\gamma = -\gamma\mathbf{A} + \mathbf{W} , \tag{13}$$

where γ is a free parameter. In what follows, we always set the on-site energy $\epsilon_D = 0$. Considering our search Hamiltonian, we can see that setting $\gamma = 1$ corresponds to a coupling strength of $v = 0$ from the perturbed vertex and its nearest-neighbors; our perturbation essentially removes the marked vertex $(\alpha_o,\beta_o)^A$ from the lattice. Note that vacancies are a common, naturally occurring, defects in graphene lattices [22].

In order to establish the critical value of γ, we numerically calculate the spectrum of $\mathbf{H}_\gamma$ as a function of γ, plotted in Figure 3 for a torus of dimensions $m = n = 12$. As $\mathbf{W}$ is a rank-2 perturbation, we see in Figure 3 two perturber states working their way through the spectrum to an avoided crossing around $\epsilon_D = 0$ when $\gamma = 1$, that is, when the perturbed vertex is removed from the underlying lattice.

As well as establishing a critical value for γ, we also find from this figure the states involved in the avoided crossing: the four Dirac states at the Dirac energy and the two perturber states which form our perturbation matrix $\mathbf{W}$. However, with further consideration, we may reduce the number of states involved further. As we have removed the site $(\alpha_0,\beta_0)^A$ from the lattice it can no longer interact with the rest of the lattice and the corresponding state drops out. Also, by direct calculation one finds that the B-type Dirac states do not interact with the perturbation, that is, $\mathbf{W}\left|\underline{K}\right\rangle^B = \mathbf{W}\left|\underline{K}'\right\rangle^B = 0$. Thus, they remain an eigenstate of the search Hamiltonian and do not interact with the perturbation. We are left with three states taking part in the avoided crossing: $\{\left|\underline{K}\right\rangle^A, \left|\underline{K}'\right\rangle^A, \left|\ell\right\rangle\}$.

We reduce our search Hamiltonian in this three state basis at the critical point $\gamma = 1$ to obtain the following reduced Hamiltonian describing the local dynamics at the

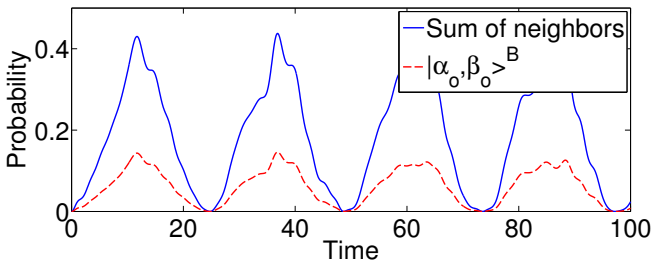


FIG. 4. (Color online) Search on 12×12 cell graphene lattice with a triple-bond perturbation, using starting state $|s\rangle$ from Equation 17. For tori with $m = n$ the dynamics at each neighboring site is the same so only one is shown.

avoided crossing

$$\tilde{\mathbf{H}} = \sqrt{\frac{6}{N}} \begin{bmatrix} 0 & 0 & e^{-i\mu_o} \\ 0 & 0 & e^{-i\nu_o} \\ e^{i\mu_o} & e^{i\nu_o} & 0 \end{bmatrix} \tag{14}$$

with $\mu_o = \frac{2\pi}{3}(\alpha_o + 2\beta_o)$ and $\nu_o = \frac{2\pi}{3}(2\alpha_o + \beta_o)$. This reduced Hamiltonian has eigenvalues $\tilde{E}_\pm = \pm 2\sqrt{\frac{3}{N}}, \tilde{E}_0 = 0$, and eigenvectors

$$\left|\tilde{\psi}_\pm\right\rangle = \frac{1}{2}\left(e^{-i\mu_o}\left|K\right\rangle^A + e^{-i\nu_o}\left|K'\right\rangle^A \pm \sqrt{2}\left|\ell\right\rangle\right) \tag{15}$$

$$\left|\tilde{\psi}_0\right\rangle = \frac{1}{\sqrt{2}}\left(e^{-i\mu_o}\left|K\right\rangle^A - e^{-i\nu_o}\left|K'\right\rangle^A\right). \tag{16}$$

Using the eigenvectors of the reduced Hamiltonian, we can construct a search starting state which is a superposition of Dirac states

$$\begin{aligned} |s\rangle &= \frac{1}{\sqrt{2}}\left(\left|\tilde{\psi}_+\right\rangle + \left|\tilde{\psi}_-\right\rangle\right) \\ &= \frac{e^{-i\mu_o}}{\sqrt{2}}\left(\left|\underline{K}\right\rangle^A + e^{-i\frac{2\pi}{3}(\alpha_o-\beta_o)}\left|\underline{K}'\right\rangle^A\right). \end{aligned} \tag{17}$$

Allowing our search starting state $|s\rangle$ to evolve under the reduced Hamiltonian we find

$$\begin{aligned} |\psi(t)\rangle &= e^{-i\tilde{\mathbf{H}}t}|s\rangle \\ &= \frac{1}{\sqrt{2}}\left(e^{-i\tilde{E}_+ t}\left|\tilde{\psi}_+\right\rangle + e^{-i\tilde{E}_- t}\left|\tilde{\psi}_-\right\rangle\right) \\ &= \cos\left(\tilde{E}_+ t\right)|s\rangle - i\sin\left(\tilde{E}_+ t\right)|\ell\rangle, \end{aligned} \tag{18}$$

so that our system rotates from our Dirac superposition $|s\rangle$ to a state which is localised on the neighbors of the perturbed vertex $|\ell\rangle$ in a time $t = \frac{\pi}{4}\sqrt{\frac{N}{3}}$. Thus, we find a $\mathcal{O}\left(\sqrt{N}\right)$ search time, a polynomial improvement over the classical search time.

We plot in Figure 4 a numerically calculated search for a lattice with $N = 288$ sites. The system has been prepared in $|s\rangle$ and allowed to evolve under the full search Hamiltonian from Eq. (13) at the critical value $\gamma = 1$. One finds that the system localises on the neighbors of the marked vertex and, for this particular system size, the probability for a measurement of the system to return one of the neighbors is around 45% at its peak. This is orders of magnitude higher than the average probability to measure other vertices in the lattice, $100/N$, which for this system size is around 0.35%. The localised state interacting with the spectrum under the full Hamiltonian has a tail into the rest of the lattice; this leads to a loss of probability to be found at the neighboring vertices below 100%.

It is worth emphasising that the marked vertex plays no role in the search - it is removed from the lattice. Rather, we force the system to localise on the nearest-neighbors, essentially making the marked vertex conspicuous by its absence. This feature differentiates our algorithm from previous searches, which have generally concentrated on localising directly on the marked vertex. An approach considering the neighboring vertices was detailed in [27], however, the focus was here still on localising on a single site but with classical post-processing steps considering the tail of the localised state extending into the neighborhood around the marked vertex.

At this point, there are a number of issues which need to be mentioned. The first is that our starting state in Eq. (17) contains information about the marked vertex in the form of the relative phase between the Dirac states. However, this phase can only take three different values. Therefore, we have three possible optimal starting states for an A-type perturbation and the same number for B-type perturbations; there are thus in total six possible optimal states. As not all of these states are orthogonal, we only find an increase of necessary runs for a successful search by a factor of 4; this additional overhead is independent of N and, therefore, does not affect the overall time complexity of the search. The particular representation of the Dirac states in Eq. (10) was chosen in such a way as to make the calculations and conceptualisation of the system dynamics easier. In reality, constructing starting states which exist on one sublattice only, experimentally is extremely difficulty; rather, in an experiment, one is likely to excite a superposition of Dirac states, reducing the success probability, on average, by a factor of 1/4.

Our search is based on the conic dispersion relation in the spectrum and the $\mathcal{O}\left(1/\sqrt{N}\right)$ scaling between successive energy levels in the linear regime, giving rise to the $\mathcal{O}\left(\sqrt{N}\right)$ search time found in our reduced model. However, previous searches in continuous-time using a modified Dirac Hamiltonian [9] or in discrete-time [7] have found logarithmic corrections to the search time. As we have seen in Eq. (18) the search time is related to the energy gap at the avoided crossing. In the inset of Figure 3 we have numerically calculated the scaling of the gap in the spectrum of the full search Hamiltonian and

we indeed find evidence for a logarithmic correction. The lack of a logarithmic term in the search time for our reduced model is due to the neglecting contributions from the rest of the spectrum.

In what follows we establish a more accurate estimate of the running time and success probability by working with the full Hamiltonian. We also justify the findings of our reduced model: while this model is insufficient to estimate the finer details, such as logarithmic correction terms, the accurate calculations show that our search algorithm indeed takes place mainly in a two-dimensional subspace spanned by the Dirac states and a state localised on the neighbors of the marked vertex.

V. QUANTUM SEARCH ON GRAPHENE - DETAILED ANALYSIS

We follow here closely our derivation as presented in [10] which builds on ideas given in [8] for a similar a similar calculation for regular rectangular lattices. We focus first on the search success amplitude, that is,

$$\langle \ell |\, e^{-i\mathbf{H}T}\, |start\rangle = \sum_{|\psi_a\rangle} \langle \ell |\, \psi_a\rangle \, \langle \psi_a |\, start\rangle \, e^{-iE_aT}, \quad (19)$$

where T is the search time, that is, the time our search probability reaches a maximum, and our search Hamiltonian $\mathbf{H}$ is given by Eq. (13) with $\gamma = 1$, that is,

$$\mathbf{H} = -\mathbf{A} + \sqrt{3}\,|\ell\rangle\,\langle \alpha_o, \beta_o| + \sqrt{3}\,|\alpha_o, \beta_o\rangle\,\langle \ell| \;; \quad (20)$$

here, $|\psi_a\rangle$, E_a are the eigenstates and eigenenergies of $\mathbf{H}$. We assume, without loss of generality, a specific starting state $|start\rangle$ where the marked vertex is chosen such that $e^{i\frac{2\pi}{3}(\alpha_o+2\beta_o)} = 1$ leading to

$$|start\rangle = \frac{1}{\sqrt{2}}\left(|\underline{K}\rangle + |\underline{K}'\rangle\right) . \quad (21)$$

In the following, we suppress the sublattice superscript as the analysis is the same regardless on which sublattice the perturbation lives. We also denote $\epsilon\,(\underline{k})$ the positive eigenenergies of $-\mathbf{A}$ from Eq. (6) and set $\epsilon_D = 0$.

For eigenstates $|\psi_a\rangle$ with eigenenergies E_a that are not in the unperturbed graphene spectrum ($E_a \neq \epsilon(\underline{k})$ for all points $\underline{k}$ in the dual lattice), we may rewrite Eq. (20) in the form

$$|\psi_a\rangle = \sqrt{3R_a}(E_a + \mathbf{A})^{-1}\,|\alpha_o, \beta_o\rangle \;, \quad (22)$$

where $\sqrt{R_a} = \langle \ell |\, \psi_a\rangle$ and the phase of $|\psi_a\rangle$ is chosen such that $\langle \ell |\, \psi_a\rangle \geq 0$.

At this point, we can remove several states from the summation in Eq. (19). Note that the basis state associated with the marked vertex, $|\alpha_o, \beta_o\rangle$, is itself an eigenstate of the search Hamiltonian with $\mathbf{H}\,|\alpha_o, \beta_o\rangle = 0$, and also, $\langle \ell |\, \alpha_o, \beta_o\rangle = 0$ so that $|\alpha_o, \beta_o\rangle$ does not contribute to the time-evolution. We may also remove eigenstates of $\mathbf{H}$ which are at the same time eigenstates of $-\mathbf{A}$ with the same energy.

This can be seen in the following way. We first consider an unperturbed eigenstate $|\psi_a^o\rangle$ such that $-\mathbf{A}\,|\psi_a^o\rangle = E_a\,|\psi_a^o\rangle$. Let us assume that there is an eigenvector $|\psi_a\rangle$ of the search Hamiltonian with the same eigenenergy E_a, that is, $\mathbf{H}\,|\psi_a\rangle = E_a\,|\psi_a\rangle$. Considering the matrix element $\langle \psi_a^o |\, \mathbf{H}\,|\psi_a\rangle$, we find $\langle \psi_a^o |\, \ell\rangle\,\langle \alpha_o, \beta_o |\, \psi_a\rangle + \langle \psi_a^o |\, \alpha_o, \beta_o\rangle\,\langle \ell |\, \psi_a\rangle = 0$. As $|\alpha_o, \beta_o\rangle$ is an eigenvector of the search Hamiltonian we know that $\langle \alpha_o, \beta_o |\, \psi_a\rangle = 0$. This leaves us with $\langle \psi_a^o |\, \alpha_o, \beta_o\rangle\,\langle \ell |\, \psi_a\rangle = 0$. As the unperturbed eigenstate $|\psi_a^o\rangle$ is simply a Bloch state we know $\langle \psi_a^o |\, \alpha_o, \beta_o\rangle \neq 0$. Thus, we obtain $\langle \ell |\, \psi_a\rangle = \sqrt{R_a} = 0$. It is then clear that eigenstates of the search Hamiltonian whose eigenenergies remain in the spectrum of $-\mathbf{A}$ do not play a role in the time-evolution of the search.

We now derive an eigenvalue condition for those perturbed eigenvalues which are in the spectrum of $\mathbf{H}$. Using the orthogonality of eigenstates $\langle \alpha_o, \beta_o |\, \psi_a\rangle = 0$, Eq. (22) leads to

$$\sqrt{3R_a}\,\langle \alpha_o, \beta_o |\,(E_a + \mathbf{A})^{-1}\,|\alpha_o, \beta_o\rangle = 0\,. \quad (23)$$

By expressing $\langle \alpha_o, \beta_o|$ in terms of the eigenstates of the *unperturbed* walk Hamiltonian $-\mathbf{A}$, we may write this as a quantization condition

$$F\,(E_a) = 0 \quad (24)$$

with

$$F\,(E) = \frac{\sqrt{3}}{N}\sum_{\underline{k}}\left[\frac{1}{E - \epsilon\,(\underline{k})} + \frac{1}{E + \epsilon\,(\underline{k})}\right] , \quad (25)$$

were N is the total number of sites in the lattice. Eq. (25) is written as two summations to incorporate the fact that the spectrum of $-\mathbf{A}$ as well as $\mathbf{H}$ is symmetric around $E = 0$.

Choosing $|\psi_a\rangle$ to be normalised $\langle \psi_a |\, \psi_a\rangle = 1$, Eq. (22) also implies

$$3R_a\,\langle \alpha_o, \beta_o |\,(E_a + \mathbf{A})^{-2}\,|\alpha_o, \beta_o\rangle = 1, \quad (26)$$

which allows R_a to be rewritten as

$$R_a = \frac{1}{\sqrt{3}|F'\,(E_a)|}. \quad (27)$$

We may now rewrite the amplitude in Eq. (19) in the form

$$\langle \ell |\, e^{-i\mathbf{H}T}\, |start\rangle = \langle \alpha_o, \beta_o |\, start\rangle \sum_a \frac{e^{-iE_aT}}{E_a|F'\,(E_a)|}\,, \quad (28)$$

where we have used the adjoint of Eq. (22). Note again that eigenstates of $\mathbf{H}$, which are also in the spectrum of $-\mathbf{A}$, do not contribute to the time-evolution of the search; it may be seen from the definition of $F\,(E)$ in Eq. (25) that $|F'\,(E_a)| \to \infty$, where E_a is in the spectrum of $-\mathbf{A}$.

As we saw in the previous section, the avoided crossing is formed by two perturbers approaching symmetrically either side of the Dirac states with energy $\epsilon_D = 0$. Thus, we concentrate on evaluating the contribution to the time-evolution from these perturbed eigenstates of $\mathbf{H}$ either side of the Dirac point and we label these states $|\psi_\pm\rangle$. In order to evaluate these contributions we calculate the perturbed eigenenergy E_+ and also derive a leading-order expression for $F'(E_+)$ (since the spectrum is symmetric, we have $E_+ = -E_- > 0$).

Using the definition of $F(E)$ in Eq. (25), we estimate $F(E_+)$ by separating out the Dirac points, where $\epsilon(\underline{K}) = \epsilon(\underline{K}') = 0$, from the summations and then Taylor expanding the remaining terms at $E = 0$, to find

$$F(E_+) = \frac{4\sqrt{3}}{NE_+} - \sum_{n=1}^{\infty} I_{2n} E_+^{2n-1}\,, \tag{29}$$

where the sums I_n are given by

$$I_n = \frac{\sqrt{3}}{N} \sum_{\underline{k} \neq \underline{K}, \underline{K}'} \left[\frac{1}{[\epsilon(\underline{k})]^n} + \frac{1}{[-\epsilon(\underline{k})]^n} \right]. \tag{30}$$

As the unperturbed spectrum is symmetric only those I_n with even n are non-zero; thus from now on we focus only on I_{2k} where $k \geq 1$.

We stated earlier that the spectrum of graphene is well-approximated by a conic dispersion relation around the Dirac points. Thus, it is from around these points that the major contributions to the I_{2k} sums arise. By applying the linear approximation from Eq. (7) and the momenta quantum numbers from Eq. (9) we may approximate the I_{2k} summations as

$$I_{2k} = 4\sqrt{3} N^{k-1} \left[\sum_{(p,q)\in L} Z_2\left(S_{\underline{K}}, 2\right) + \sum_{(p,q)\in L'} Z_2\left(S_{\underline{K}'}, 2\right) \right] + O(1)\,. \tag{31}$$

Here $Z_2(S, x)$ is the Epstein zeta-function [21]

$$Z_2(S, x) = \frac{1}{2} \sum_{(p,q)\in\mathbb{Z}^2\setminus(0,0)} \left(S_{11}p^2 + 2S_{12}pq + S_{22}q^2\right)^{-x}\,, \tag{32}$$

for a real positive definite real symmetric 2×2 matrix S. For our purposes we use

$$S_{\underline{K}} = S_{\underline{K}'} = 4\pi^2 \begin{pmatrix} 2 & -1 \\ -1 & 2 \end{pmatrix}, \tag{33}$$

which describes the spectrum close to the Dirac points. The linear approximation around both Dirac points K and K' is the same and, thus, the matrices $S_{\underline{K}}$ and $S_{\underline{K}'}$ are equal.

Our summation in Eq. (31) is over the rectangular regions L and L' of the lattice $\mathbb{Z}^2$. Both are centered on $(0,0)$ and have side lengths proportional to $\sqrt{N}$, however the center, $(0,0)$, corresponding to the relevant Dirac point, is omitted from the summation.

Convergence of the Epstein zeta function is well-known for $k \geq 2$ [21], and leads to the bounds

$$\lim_{N\to\infty} \frac{I_{2k}}{N^{k-1}} = 4\sqrt{3}\left(Z_2(S_{\underline{K}}, k) + Z_2(S_{\underline{K}'}, k)\right) \tag{34}$$

for $k \geq 2$. A sharp estimate for

$$I_2 = O(\ln N)\,. \tag{35}$$

is given in Appendix A. In order to calculate an estimate for E_+, we truncate the Taylor expansion of $F(E)$ in Eq. (29) at the I_2 term (the first term in the summation), and apply the eigenvalue condition $F(E_+) = 0$. That is, we solve $\frac{4\sqrt{3}}{NE_+} - I_2 E_+ = 0$ and obtain the approximation $E_+^2 \approx \frac{4\sqrt{3}}{NI_2}$. This solution also leads to the estimate $F'(E_+) \approx -2I_2$.

We consider next whether our solution for E_+ lies inside the radius of convergence of the Taylor expansion. We note that each term in $Z_2\left(S_{\underline{K}}, k\right)$ is smaller than the corresponding term in $Z_2\left(S_{\underline{K}}, 2\right)$ for $k > 2$, and so it follows that $Z_2(S_{\underline{K}}, k) < Z_2(S_{\underline{K}}, 2)$ for $k > 2$. This property of the Epstein zeta function and the estimate from Eq. (34) imply

$$\sum_{n=2}^{\infty} I_{2n} E_+^{2n-1} < \frac{C}{NE_+} \sum_{n=2}^{\infty} (NE_+^2)^n$$

i.e. the infinite sum in Eq. (29) converges for $E_+ < 1/\sqrt{N}$. Thus, for large N, our solution lies within the radius of convergence of our Taylor expansion in Eq. (29).

In order to show that the dominant contributions to the search come from $|\psi_\pm\rangle$, we need to establish the leading order error term. All the I_{2k} sums are positive so that, given the sign of all the terms in the Taylor expansion in Eq. (29), the true value of $E_+ > 0$ has to be smaller than the estimate we have obtained. Thus, we write the true value of E_+ as

$$E_+^2 = \frac{4\sqrt{3}}{NI_2} - \Delta > 0\,, \tag{36}$$

with $\Delta > 0$. One may rewrite $F(E_+) = 0$, using the true value of E_+, to give

$$I_2\Delta = \sum_{n=2}^{\infty} I_{2n} E_+^{2n}\,. \tag{37}$$

We follow the same arguments as used for the calculation of the radius of convergence to obtain an upper bound for the summation. This together with the already established fact that E_+ is inside this radius for sufficiently large N, we get the following inequality:

$$0 < NI_2\Delta < C\sum_{n=2}^{\infty} (NE_+^2)^n = \frac{CN^2E_+^4}{1 - NE_+^2} = O(I_2^{-2}).$$

So $\Delta = O(I_2^{-3}N^{-1}) = O\left((\ln N)^{-3}N^{-1}\right)$. Thus, we obtain

$$E_+^2 = \frac{4\sqrt{3}}{NI_2}\left(1 + O((\ln N)^{-2})\right) . \tag{38}$$

It also follows that

$$F'(E_\pm) = -2I_2 + O\left(\frac{1}{\ln N}\right). \tag{39}$$

This shows that our perturbed eigenstates $|\psi_\pm\rangle$ have an $O(1)$-overlap with the starting state and are, therefore, the relevant states to be considered in the time-evolution of the algorithm. Using the definitions of $|\psi_a\rangle$ and R_a in Eqs. (22), (27), the inner product of the starting state and the perturbed eigenvectors can be expressed as

$$\langle start|\ \psi_a\rangle = \frac{1}{E_a}\sqrt{\frac{\sqrt{3}}{|F'(E_a)|}}\,\langle start|\ \alpha_o, \beta_o\rangle\ , \tag{40}$$

where $\langle start|\ \alpha_o, \beta_o\rangle$ is the overlap of the starting state with the marked vertex state. Applying our previous approximations for E_+ and $F'(E_+)$, that is, for our perturbed eigenstates closest to the Dirac point, we find

$$|\langle start|\ \psi_\pm\rangle| = \frac{1}{\sqrt{2}} + O\left(\frac{1}{\ln^2 N}\right). \tag{41}$$

Thus, our starting state is indeed a superposition of the perturbed eigenstates, $|\psi_\pm\rangle$ as assumed in the previous section. This makes it possible to investigate the running time and success amplitude of the algorithm in more detail, that is,

$$\left|\langle \ell|\, e^{-iHt}\,|start\rangle\right| \tag{42}$$

$$\approx \left|\frac{1}{\sqrt{2}}\left(e^{-iE_+t}\,\langle \ell|\ \psi_+\rangle - e^{iE_+t}\,\langle \ell|\ \psi_-\rangle\right)\right| \tag{43}$$

$$= \frac{1}{3^{\frac{1}{4}} I_2^{\frac{1}{2}}}\,|\sin(E_+t)|\ . \tag{44}$$

It is clear from our earlier results for $E_\pm$ and I_2 that our algorithm localises on the neighbor state $|\ell\rangle$ in time $T = \frac{\pi}{2E_+} = O\left(\sqrt{N\ln N}\right)$ with probability amplitude $O\left(1/\sqrt{\ln N}\right)$. This confirms the logarithmic correction observed numerically and displayed in the inset of Fig. 3.

VI. COMMUNICATION

It has been demonstrated in [17] that discrete-time search algorithms can be modified to create a communication protocol. We show here that a communication setup can be established also in the continuous-time search algorithm with minor changes due to the subtleties of our search.

We use the same unperturbed walk Hamiltonian as before, that is, $\mathbf{H_0} = -\mathbf{A}$ and the same type of perturbation matrix as in Eq. (11), but now at two different sites in the lattice. Explicitly, our communication Hamiltonian is

$$\mathbf{H} = -\mathbf{A} + \mathbf{W_s} + \mathbf{W_t}\,, \tag{45}$$

where the perturbation matrices $\mathbf{W_{s/t}}$ mark the source and target sites, respectively.

As prescribed in [17], the communication protocol operates by preparing a state localised on the source perturbation, in our case on the neighbors of the source site, and allowing the system to evolve under our communication Hamiltonian. The system then localises on the neighboring vertices of the target site. The effect of the two perturbation matrices $\mathbf{W_{s/t}}$ amounts to disconnecting the two vertices from the underlying lattice.

As noted before, our search algorithm has several different optimal starting states depending on the position of the marked vertices. Therefore, we divide our communication analysis into three different cases: the two sites i) are on the same sublattice and have the same optimal search starting state; ii) are on the same sublattice but *do not* share the same optimal search starting state; iii) are on different sublattices. Both of the first two cases can be treated by applying the reduced Hamiltonian method demonstrated earlier, but communication between different sublattices is not tractable by this method and so we focus on numerics in this case.

For signal transfer between two sites on the same sublattice, we will assume, without loss of generality, that our communication takes place between two sites on the A-sublattice, $(\alpha_{s/t}, \beta_{s/t})^A$; here, the subscript s or t denotes the source or target vertices respectively. Using arguments as employed in Sec. IV, we can reduce the number of relevant states. Ultimately, the search dynamics takes place in the subspace spanned by the basis $|\underline{K}\rangle^A$, $|\underline{K}'\rangle^A$, the A-type Dirac states, and $|\ell_s\rangle, |\ell_t\rangle$, the uniform superpositions over the neighbors of the source and target vertices. This basis leads to the reduced Hamiltonian

$$\tilde{\mathbf{H}} = \sqrt{\frac{6}{N}}\begin{pmatrix} 0 & 0 & e^{i\mu_s} & e^{i\mu_t} \\ 0 & 0 & e^{i\nu_s} & e^{i\nu_t} \\ e^{-i\mu_s} & e^{-i\nu_s} & 0 & 0 \\ e^{-i\mu_t} & e^{-i\nu_t} & 0 & 0 \end{pmatrix}, \tag{46}$$

where $\mu_{s/t} \equiv \frac{2\pi}{3}\left(\alpha_{s/t} + 2\beta_{s/t}\right)$ and $\nu_{s/t} \equiv \frac{2\pi}{3}\left(2\alpha_{s/t} + \beta_{s/t}\right)$.

In the first case considered we assume that there are two perturbations on the graphene lattice located at the points $(\alpha_s, \beta_s)^A$ and $(\alpha_t, \beta_t)^A$, chosen such that $e^{i\frac{2\pi}{3}(\alpha_s + 2\beta_s)} = e^{i\frac{2\pi}{3}(\alpha_t + 2\beta_t)}$. This implies that a search for either vertex, using our search algorithm from Secs. IV & V, would use the same optimal starting state. As the phases are equal, we drop the subscript on the perturbation coordinates in what follows. Fixing our phases

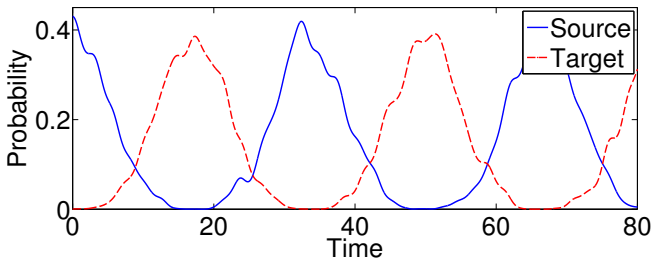


FIG. 5. (Color online) Numerically calculated signal transfer on a 12×12 cell graphene lattice between equivalent vertices, using the communication Hamiltonian in Eq. (45). The system is initialised in $|\ell_s\rangle$ and localises on $|\ell_t\rangle$. Only the sum of probabilities to be found on the neighbor vertices is shown.

and diagonalising the reduced Hamiltonian, we find it has eigenvalues $\lambda_2^{\pm} = \pm 2\sqrt{\frac{6}{N}}$ and $\lambda_0^{1,2} = 0$ with eigenvectors

$$\left|\tilde{\psi}_{\pm 2}\right\rangle = \frac{1}{2}\left(e^{i\mu}\left|\underline{K}\right\rangle^A + e^{i\nu}\left|\underline{K}'\right\rangle^A \pm |\ell_s\rangle \pm |\ell_t\rangle\right) \quad (47)$$

$$\left|\tilde{\psi}_0^1\right\rangle = \frac{1}{\sqrt{2}}\left(e^{i\mu}\left|\underline{K}\right\rangle^A - e^{i\nu}\left|\underline{K}'\right\rangle^A\right) \quad (48)$$

$$\left|\tilde{\psi}_0^2\right\rangle = \frac{1}{\sqrt{2}}\left(|\ell_s\rangle - |\ell_t\rangle\right) . \quad (49)$$

Using these eigenstates, we may rewrite the source neighbor state as

$$|\ell_s\rangle = \frac{1}{2}\left(\left|\tilde{\psi}_2\right\rangle - \left|\tilde{\psi}_{-2}\right\rangle\right) + \frac{1}{\sqrt{2}}\left|\tilde{\psi}_0^2\right\rangle . \quad (50)$$

Placing the system in the source state $|\ell_s\rangle$ and allowing the system to evolve under the reduced Hamiltonian, one finds

$$|\psi(t)\rangle = e^{-i\tilde{\mathbf{H}}t}|\ell_s\rangle \quad (51)$$

$$= \frac{1}{2}\left(e^{-i\lambda_2^+ t}\left|\tilde{\psi}_2\right\rangle - e^{-i\lambda_2^- t}\left|\tilde{\psi}_{-2}\right\rangle\right) + \frac{1}{\sqrt{2}}\left|\tilde{\psi}_0^2\right\rangle \quad (52)$$

$$= \frac{-i}{2}e^{i\mu}\sin\left(\lambda_2^+ t\right)\left(\left|\underline{K}\right\rangle^A + e^{i\frac{2\pi}{3}(\alpha-\beta)}\left|\underline{K}'\right\rangle^A\right) + \frac{1}{2}\left(\cos\left(\lambda_2^+ t\right)+1\right)|\ell_s\rangle + \frac{1}{2}\left(\cos\left(\lambda_2^+ t\right)-1\right)|\ell_t\rangle . \quad (53)$$

We note that, in the last line above, the term in the brackets involving only the Dirac states is actually the optimal search starting state for both perturbed vertices, defined in Eq. (17). The system thus oscillates between the states localised on the neighbors of the perturbed vertices, $|\ell_s\rangle$ and $|\ell_t\rangle$, in a time $T = \frac{\pi}{2}\sqrt{\frac{N}{6}}$, via their optimal search starting state.

Figure 5 shows the system evolving under the full communication Hamiltonian, Eq. (45). The initial state used for the time evolution shown in Figure 5 is the true localised state, that is, we run the quantum search with a single perturbation located at vertex $(\alpha_s, \beta_s)^A$ until it reaches maximum success probability, and then apply the second perturbation to the vertex $(\alpha_t, \beta_t)^A$. The figure confirms the behaviour expected from the reduced model calculation.

The communication mechanism essentially works in the same way as the quantum search algorithm, as it can be viewed as one marked vertex 'finding' another. The initial localised source state decays back towards the search starting state, and the system then searches for the target state.

In our second case of signal transfer we analyse the behaviour of a communication system where we have two perturbed vertices on the same sublattice, but with the restriction that $e^{i\frac{2\pi}{3}(\alpha_s+2\beta_s)} \neq e^{i\frac{2\pi}{3}(\alpha_t+2\beta_t)}$. As such, the two marked sites cannot interact via the same search starting state. However, the optimal search starting states are not orthogonal so that signal transfer is still possible, but the resulting interference effects make the analysis slightly more complicated.

We rewrite the coordinates of the target in terms of the source, $\alpha_t = \alpha_s + x$ and $\beta_t = \beta_s + y$. Again, fixing our phases and diagonalising the reduced Hamiltonian in Eq. (46), we find it has eigenvalues $\lambda_{\sqrt{3}}^{\pm} = \pm\sqrt{3}\sqrt{\frac{6}{N}}$ and $\lambda_1^{\pm} = \pm\sqrt{\frac{6}{N}}$ with eigenvectors

$$\left|\tilde{\psi}_{\pm\sqrt{3}}\right\rangle = \frac{e^{i\mu_s}}{2\sqrt{3}}\left(e^{i\frac{2\pi}{3}(x+2y)}-1\right)\left|\underline{K}\right\rangle^A + \frac{e^{i\nu_s}}{2\sqrt{3}}\left(e^{-i\frac{2\pi}{3}(x+2y)}-1\right)\left|\underline{K}'\right\rangle^A \mp \frac{1}{2}|\ell_s\rangle \pm \frac{1}{2}|\ell_t\rangle \quad (54)$$

$$\left|\tilde{\psi}_{\pm 1}\right\rangle = \mp\frac{e^{i\mu_s}}{2}\left(e^{i\frac{2\pi}{3}(x+2y)}+1\right)\left|\underline{K}\right\rangle^A \pm \frac{e^{i\nu_s}e^{i\frac{2\pi}{3}(x+2y)}}{2}\left|\underline{K}'\right\rangle^A - \frac{1}{2}|\ell_s\rangle - \frac{1}{2}|\ell_t\rangle . \quad (55)$$

Using these eigenstates, one may write the source perturbation as

$$|\ell_s\rangle = \frac{1}{2}\left(-\left|\tilde{\psi}_{\sqrt{3}}\right\rangle + \left|\tilde{\psi}_{-\sqrt{3}}\right\rangle - \left|\tilde{\psi}_1\right\rangle - \left|\tilde{\psi}_{-1}\right\rangle\right) . \quad (56)$$

The full expression for the time-evolution is rather cumbersome; therefore, we only show the terms and prefactors we are interested in, namely $|\ell_s\rangle$ and $|\ell_t\rangle$

$$|\psi(t)\rangle = \frac{1}{2}\left[\cos\left(\lambda_{\sqrt{3}}^+ t\right) + \cos\left(\lambda_1^+ t\right)\right]|\ell_s\rangle - \frac{1}{2}\left[\cos\left(\lambda_{\sqrt{3}}^+ t\right) - \cos\left(\lambda_1^+ t\right)\right]|\ell_t\rangle . \quad (57)$$

We can see here that the prefactors do not depend upon the coordinates of either the source or the target sites; the transport signal between sites on the same sublattice but with different optimal search starting state is thus independent of the position of the source or target site.

In Figure 6 we show the system evolved under the full communication Hamiltonian. Again, the initial state is the true localised state on the nearest-neighbors of the

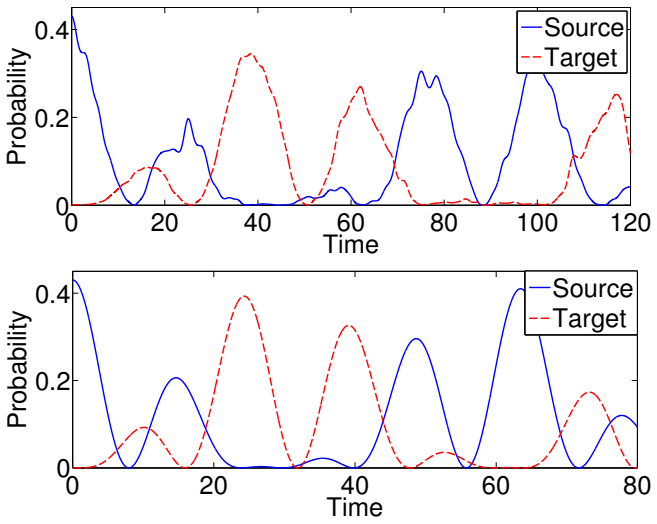


FIG. 6. (Color online) Upper: Numerically calculated signal transfer on a 12×12 cell graphene lattice between non-equivalent vertices, using the communication Hamiltonian in Eq. (45). The system is initialised in $|\ell_s\rangle$ and localises on $|\ell_t\rangle$. Only the sum of probabilities to be found on the neighbor vertices is shown. Lower: Analytically calculated behaviour for the same system, using the reduced Hamiltonian method and Eq. (57).

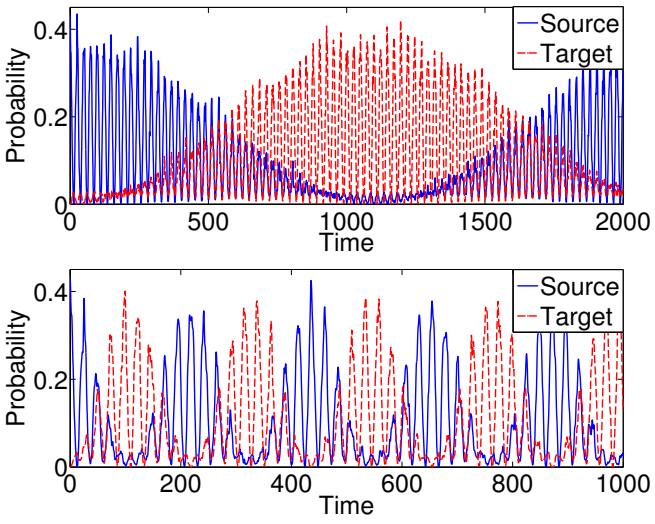


FIG. 7. (Color online) Numerically calculated signal transfer on a 12×12 cell graphene lattice between vertices on different sublattices, using the communication Hamiltonian in Equation 45. The system is initialised in $|\ell_s\rangle$ and localises on $|\ell_t\rangle$. Only the sum of probabilities to be found on the neighbor vertices is shown. The two figures have the same source position but different positions of the target site.

source vertex, obtained by running the search algorithm using one marked vertex until it reaches its peak success probability. The time-evolution is radically different to the previous communication case; the behaviour here is erratic with uneven peaks of probability at the two perturbations involved in the protocol. However, there are still significant probability revivals.

The transport behaviour from Eq. (57), calculated using the reduced Hamiltonian, is also shown in Figure 6. The probability at time $t = 0$ has been scaled to match that shown in Figure 6. Our calculated behaviour has the same signal pattern as the numerically calculated behaviour from the full Hamiltonian, although over a shorter period of time. As our reduced model only makes use of the Dirac states and the perturber states, we lose the contribution to the time-evolution from the rest of the spectrum giving rise to logarithmic corrections as discussed in Sec. V. This leads to differences in the overall time scales for the reduced model and the full Hamiltonian. This also supports our findings that signal transfer between all non-equivalent vertices on the same sublattice is the same. The communication protocol is again set up by a search mechanism in reverse, where one vertex finds another. The slightly erratic behaviour that emerges here is due to interference between the two separate search mechanisms which interact due to the non-zero inner product of the three possible optimal search starting states for vertices on the A-sublattice.

In our final case of signal transfer, we consider communication between sites on different sublattices which we can not treat in the reduced Hamiltonian model. It has been demonstrated previously that perturbations to one sublattice do not interact with the Dirac states which live on the other sublattice. Therefore, when attempting to reduce the communication Hamiltonian as done before, we merely find that it decouples into two non-interacting reduced Hamiltonians, each describing a search protocol on one sublattice. The interaction between the two sublattices is here facilitated due to interactions via the bulk of the spectrum. In what follows, we focus on numerics and inspect the behaviour for systems involving the same source perturber but different targets. The numerics show a finite number of different signal patterns, two examples are shown in Figure 7. We can see from these examples that the communication mechanism takes place over a much longer timescale with a superimposed oscillatory dynamics.

The increase in timescale can be attributed to the weak nature of the interaction between the two perturbations due the fact that the localised states live mainly on one sublattice. The signal pattern in Figure 7 thus decouples into a fast oscillation between one site, say the source site, and the delocalised lattice state and a slow time scale on which a small amount of probability amplitude escapes into the other sublattice due to the weak interaction. This process continues until the recurrence probability at the target perturbation reaches the same peak as the initial localised source state, and then the behaviour reverses.

VII. ALTERNATIVE METHODS OF MARKING

In the previous sections, we have discussed a method of marking a vertex through modifying the hopping potential from the perturbed site to all three of its nearest-neighbors. Here, we will discuss alternative methods of marking a vertex which still keep the perturber interaction in the conic dispersion region of the spectrum. This can be done by altering the hopping potential in different ways as discussed above; this approach is necessarily a rank-2 perturbation and these two perturber states must meet at the Dirac energy. We will discuss several ways of applying such a perturbation in the next paragraph. Another approach is based on coupling extra sites to the lattice; this set-up will be discussed at the end of this section.

Focussing on hopping potential perturbations, we may consider perturbing the bonds to any number of nearest-neighbors to any strength. We have seen previously that a symmetric three-bond perturbation successfully creates a search. Here, we demonstrate a search based on perturbing the hopping potential from a given site to only one of its nearest-neighbors. That is, we use the same search Hamiltonian as in Eq. (13) with the perturbation matrix

$$\mathbf{W} = |\alpha_o, \beta_o\rangle^A \langle \alpha_o, \beta_o|^B + |\alpha_o, \beta_o\rangle^B \langle \alpha_o, \beta_o|^A , \quad (58)$$

and eigenstates

$$|W_g\rangle = \frac{1}{\sqrt{2}} \left(|\alpha_o, \beta_o\rangle^A - |\alpha_o, \beta_o\rangle^B \right) \quad (59)$$

$$|W_e\rangle = \frac{1}{\sqrt{2}} \left(|\alpha_o, \beta_o\rangle^A + |\alpha_o, \beta_o\rangle^B \right). \quad (60)$$

Note that it no longer makes sense to speak of a single marked vertex. Rather, our perturbation marks both vertices $(\alpha_o, \beta_o)^{A/B}$ simultaneously; thus, it may be more accurate to view our perturbation matrix as marking a single cell of the lattice.

For this type of perturbation, the avoided crossing used to generate search behaviour is not necessarily at $\gamma = 1$, see Figure 8, where the spectrum of our search Hamiltonian as a function of γ for a 12×12 cell torus is shown. As stated before, our single bond perturbation is also a rank-2 matrix, and so again there are two perturber states approaching the spectrum from the negative and positive regions of the spectrum. Inspecting the region around the Dirac energy, see inset in Figure 8, we see that avoided crossings are formed by four states in total, the two blue (solid) curves and the two red (dashed) curves. At $\gamma = \frac{1}{3}$ there is an exact crossing between the red and blue curves indicating that these states are orthogonal.

We can make this avoided crossing picture clearer by breaking down the eigenstates of the search Hamiltonian in terms of the symmetries of the lattice. In particular, we use the rotation operator C_2, which is a rotation of π about the mid-point of the perturbed bond. Considering the action of C_2 on the marked vertices and

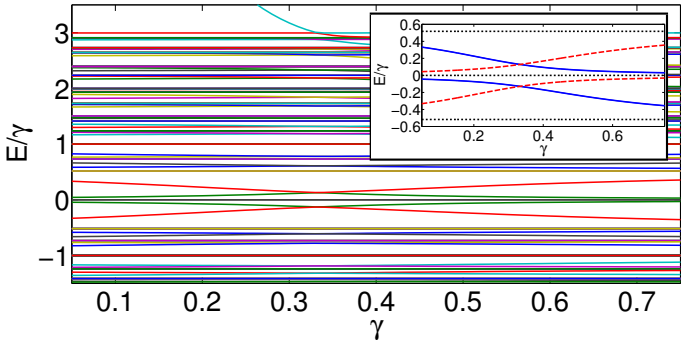


FIG. 8. (Color online) Spectrum of single-bond search Hamiltonian in Eq. (13) using perturbation from Eq. 58 as a function of γ for a 12×12 cell torus ($N = 288$). The spectrum is symmetric around $\epsilon_D = 0$. Inset: States nearest the Dirac energy have been coloured depending on their parity with respect to the C_2 operator: even (solid blue), odd (dashed red), undefined (dot-dashed black).

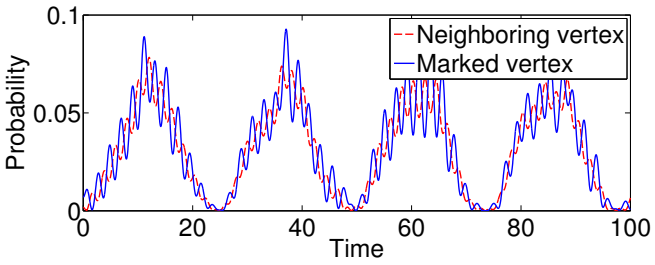


FIG. 9. (Color online) Search on 12×12 cell graphene lattice with single-bond perturbation, using an optimal starting state. The behaviour at both marked vertices is the same, as is the behaviour at each of their neighboring sites.

the eigenstates of the perturbation matrix, one finds $C_2 |\alpha_o, \beta_o\rangle^{A/B} = |\alpha_o, \beta_o\rangle^{B/A}$, $C_2 |W_g\rangle = -|W_g\rangle$ and $C_2 |W_e\rangle = |W_e\rangle$. The inset of Figure 8 shows the states nearest to the Dirac energy, where the same colour indicates the same C_2 parity. It now becomes clear that the states near the Dirac point actually form two avoided crossings, one for each parity with a minimum energy gap at $\gamma = \frac{1}{3}$.

Without going into details, we can again find optimal starting states using a reduced Hamiltonian approach (one for each of the avoided crossings); the evolution of the system using these optimal states is shown in Figure 9 for a 12×12 cell lattice. We find there is a significant localisation on the marked vertices and their nearest-neighbors, with the probability of being found on either of the marked vertices peaking at around $16 - 18\%$. We can also see that the probability of being found on each of the nearest-neighbors peaks at around 8%, resulting in a total probability of being found on the marked vertices and their nearest-neighbors of approximately 48%. The success probability fluctuates, as the probability amplitude oscillates between the marked vertices and their nearest-neighbors. This is due to the probability ampli-

tude being constrained in the local area by the increased hopping potential between the two marked vertices.

Although our demonstration is for a 12×12 cell lattice, numerical investigations show that the search behaviour remains the same as the lattice size increases with critical value fixed at $\gamma = \frac{1}{3}$. We also find that the gap at the two avoided crossings scales as $\mathcal{O}\left(1/\sqrt{N\ln N}\right)$, in the same way as for the three-bond perturbation shown in Figure 3. As the search time is inversely proportional to the energy splitting at the avoided crossing, it also gives an estimate of the running time of the search $T = \mathcal{O}\left(\sqrt{N\ln N}\right)$.

We now turn to coupling additional sites to the lattice as a way of introducing a perturbation as also considered in [12]; such a treatment is in many ways closer to experimental realisations as defects due to additional add-on atoms are quite common in graphene [23]. We focus here on the idealised case where an additional site is coupled to a single lattice vertex. We use the perturbation matrix

$$\mathbf{W}(\gamma) = -\left|\alpha_o,\beta_o\right\rangle^A\langle site| - |site\rangle\left\langle\alpha_o,\beta_o\right|^A + \gamma\,|site\rangle\langle site|\,, \tag{61}$$

for coupling the additional site $|site\rangle$ to the A-type vertex $(\alpha_o,\beta_o)^A$ and γ is a free parameter related to the on-site energy of the additional vertex. The choice of the coupling terms is such that the binding energy between the additional site and the lattice vertex is the same as the internal couplings in the lattice. Thus, our search Hamiltonian is of the form

$$\mathbf{H} = -\mathbf{A} + \mathbf{W}(\gamma)\,. \tag{62}$$

In Figure 10, the spectrum of the search Hamiltonian is given as function of γ. As our free parameter γ only changes a single term, our spectrum only has a single perturber state. One finds a clear avoided crossing around the Dirac energy ($E = 0$) when $\gamma = 0$, that is, when the on-site energy of the additional site matches the on-site energy of the lattice vertices.

In the reduced Hamiltonian picture, we write Eq. 62 in terms of a basis consisting of the Dirac states and our perturber state, $|site\rangle$. Only three states are involved in the search, that is, $\{\left|\underline{K}\right\rangle^A, \left|\underline{K}'\right\rangle^A, |site\rangle\}$, and $\mathbf{H}$ reduces, up to a different prefactor, to the same 3×3 matrix found in Eq. (14) for the three-bound perturbation. Thus, our previous reduced Hamiltonian analysis holds for this case and the optimal search starting states are the same; the time-evolution for the additional site search is shown in the inset in Figure 10. The only differences between this case and the three-bond marking are that the system localises on the additional site, and also the change in prefactor leads to a search time of $T = \frac{\pi}{4}\sqrt{N}$.

We note that other, more realistic types of perturbations involving additional sites coupling to a lattice site and its neighbors, can be shown to result in effective search protocols. Also, the single additional site perturbation described here can, like the three-bond perturbation, be used to setup a communication protocol, with the same signal patterns and behaviours as found previously. The initial state is in this case completely localised on the additional site.

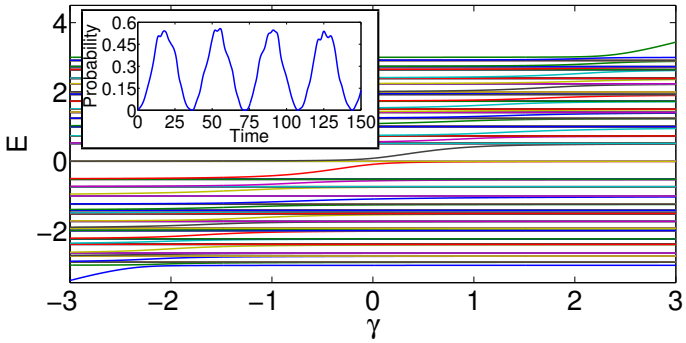


FIG. 10. (Color online) Spectrum of the Hamiltonian in Eq. (62) as a function of γ for a 12×12 cell torus ($N = 288$). The symmetry of the graphene spectrum is broken by the choice of the perturbation in terms of an additional site. Inset: Search on 12×12 cell graphene lattice with a single additional site perturbation, using starting state $|s\rangle$ from Eq. (17)

VIII. ALTERNATIVE NANOSTRUCTURES

So far we have described the dynamics of searches on graphene lattices with periodic boundary conditions, that is, graphene on a torus. Here we consider more realistic boundary conditions such as nanotubes and graphene sheets.

For the dynamics on nanotubes, we move to periodic boundary condition along one axis only and impose Dirichlet boundary conditions along the other directions. The properties of nanotubes are well-known [24], and it has been shown that the band structure of armchair nanotubes, that is, nanotubes with armchair boundaries, always allows for an energy at the Dirac energy regardless of the nanotube diameter; we will focus on these types of nanotubes. We are interested in searching on finite length nanotubes, where the band structure becomes discrete; the length of the nanotube are in addition chosen such that there exists an eigenenergy at the Dirac energy. An example of the cell we use to construct finite armchair nanotubes is shown in Figure 11. We choose the finite length of the nanotube to be along the horizontal axis and we close the underlying graphene lattice into a nanotube along the vertical axis.

We denote the basis states of sites in our nanotube as $|m, A/B, l\rangle$, where m indicates the m^{th} A/B-type vertex in the horizontal direction in the l^{th} cell. It is simple to see that, due to the periodic boundary conditions along the circumference of the tube, the vertical component of the eigenstates must be Bloch states and the horizontal component of the amplitudes must be sinusoidal in nature. That is, the eigenstates of the finite nanotube are standing waves along its length.

By working through the tight-binding model for this

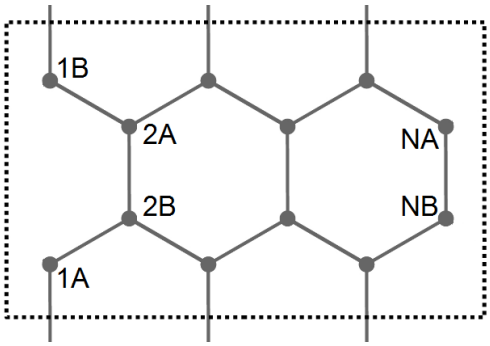


FIG. 11. Example of a armchair nanotube cell. The nanotube is periodic along the vertical axis and finite in the horizontal direction with a width of N_x sites.

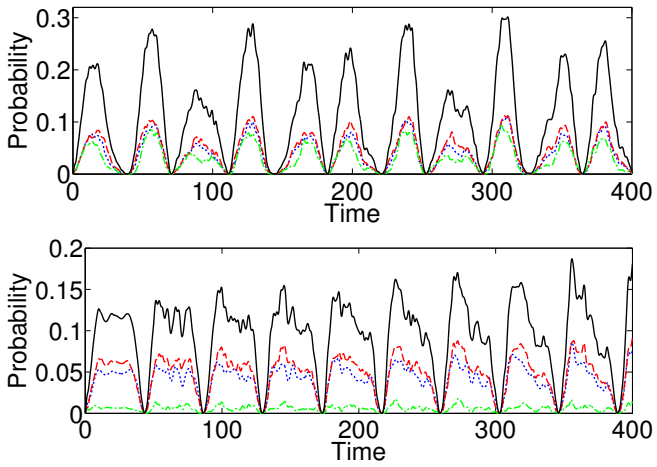


FIG. 12. (Color online) Searches on an armchair nanotube ($N = 320$) with triple-bond perturbation located in the bulk (upper figure) and placed near the edge of the nanotube(lower figure), using numerically calculated optimal starting state: $|m_o - 1, B, l_o\rangle$ (dotted blue), $|m_o + 1, B, l_o\rangle$ (dashed red), $|m_o, B, l_o\rangle$ (dot-dashed green), sum of neighbor probabilities (solid black).

system, one can show that $(k_x, k_y) = \left(\frac{2\pi}{3}, 0\right)$ is the only point where there exists an eigenenergy equal to the Dirac energy. It is also possible to show that the spectrum includes Dirac points when the number of sites along the length of the nanotube $N_x = 3r-1$, where r is an integer.

As there is only one potential Dirac point for finite armchair nanotubes, it follows that there are only two Dirac states (one from the bonding and the anti-bonding regions of the spectrum). As we have $k_y = 0$ at the Dirac point, the Bloch wave around the circumference of the nanotube is simply a uniform superposition. Another important feature of the Dirac states on the nanotube, which we have not encountered previously, is the existence of nodal points where the amplitude of the eigenstate is 0. We find these nodal points occur at every third site along the horizontal axis.

We focus on applying our three-bond perturbation from Sections IV & V to the armchair nanotube. In our new labelling our perturbation takes the form

$$W = |m_o, A, l_o\rangle \left(\langle m_o + 1, B, l_o| + \langle m_o - 1, B, l_o| + \langle m_o, B, l_o|\right) + h.c.\,. \tag{63}$$

We have assumed that we are perturbing an A-type vertex on an even horizontal coordinate, so that the perturbed site and its nearest-neighbors remain within one nanotube cell. While it is easy to re-write this perturbation matrix for other sites we restrict ourselves to this form for simplicity. Note even in this form it can still be expressed in terms of a marked site, $|m_o, A, l_o\rangle$, and a state which lives on the neighbors, $|\ell\rangle = \frac{1}{\sqrt{3}}\left(|m_o + 1, B, l_o\rangle + |m_o - 1, B, l_o\rangle + |m_o, B, l_o\rangle\right)$.

Our search Hamiltonian for the nanotube is the same as in Eq. (13). Inspecting the spectrum of the search Hamiltonian as a function of the free parameter γ where the perturbation is not located on a nodal point of a Dirac state, one finds an avoided crossing around the Dirac energy when $\gamma = 1$. This spectrum is very similar to the one shown in Figure 3 for the search on the torus and will be omitted. If the perturbation is located on a nodal site the picture is different, however; one finds that there is an exact crossing at the Dirac energy when $\gamma = 1$ and searching is not possible. Recall that the effect of the perturbation at the critical point is to completely remove the site from the lattice, if the site already has zero amplitude then the perturbation will not interact with the Dirac state.

Similar to the previous section, we numerically reduce the full search Hamiltonian in a basis consisting of the two Dirac states and the state living purely on the neighbors, $|\ell\rangle$. The perturbed site, $|m_o, A, l_o\rangle$, is decoupled from the lattice. Through this process, we find two possible starting states, one for each sublattice. The starting states are weighted superpositions of the Dirac states over the sublattice containing the marked vertex. The nodal points are excluded from this treatment.

Figure 12 shows the system evolution for two searches using the numerically found optimal starting states. One search has the marked site located in the centre of the nanotube, the other has the marked site positioned near the edge of the nanotube. The dimensions of the nanotube have been chosen so that there are 320 sites, comparable to the searches shown in earlier sections. Comparing these searches to the three-bond perturbation search on the torus in Figure 4, we see that there is a marked difference in behaviour and success probability induced by relaxing the periodic boundary conditions along one axis.

Using a perturbation located near the edge, the lower image in Figure 12, we see a reduction in success probability by a factor of 2-3 and strong fluctuations in peak height when compared to the search on the torus. Searching in the bulk, shown in the lower image of Figure 12, displays behaviour closer to searches on a graphene torus, but again with significant fluctuations at each peak. We

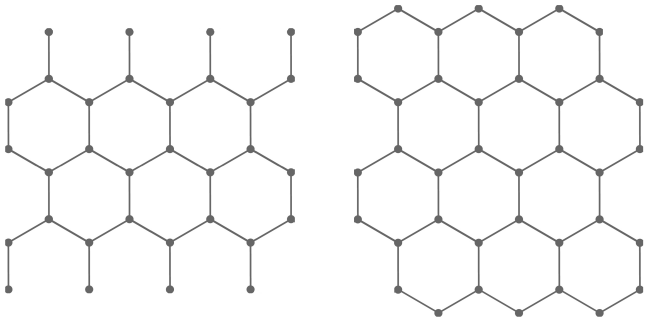


FIG. 13. Examples of two finite graphene sheets, with dimensions in terms of primitive cells $(N_x, N_y) = (4, 4)$. Along the vertical axis of both sheets are armchair edges. The horizontal boundaries are formed by bearded edges (left) and zigzag edges (right).

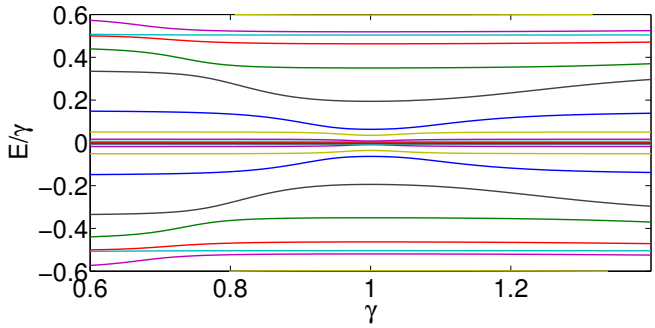


FIG. 14. (Color online) Spectrum of triple-bond perturbation search Hamiltonian in Equation 13 as a function of γ for a 10×10 cell bearded graphene sheet (N = 200). We focus only on the relevant section of the spectrum.

propose that this effect is due to the reflection of probability amplitude from the edges of the nanotube. This is supported by the changes in the interference pattern in the signal as the perturbation is moved across the lattice. Numerics demonstrate that additional site perturbations and communication protocols can also be used on nanotube lattices.

We now move to working on graphene sheets, that is, removing the periodic boundary conditions along both axis. A detailed account of a specific version of this set-up together with experimental results has been presented in [12] for graphene sheets consisting of armchair boundaries only. Note that such a configuration can not be achieved on rectangular sheets; the simplest configuration has the form of a parallelogram, see [12] for further details. The advantage of such a configuration is that the form of the boundary does not admit so-called 'edge-states'. In the following, we will look at the influence of these edge-states in more detail by considering rectangular graphene sheets, such as in Figure 13. In addition to armchair edges, here along the vertical axis, these sheets have boundaries formed by bearded edges (left) and zigzag edges (right) along the horizontal axis. These boundaries support edge states, i.e. states localised along these edges, with an eigenenergy close to the Dirac energy [25, 26]. In the following, we will investigate, how the existence of these edge states influences the search.

As in the case of the finite armchair nanotube, the imposition of Dirichlet boundary conditions at an edge generates sinusoidal eigenstates. As a result, there are no extended (bulk) eigenstates at the Dirac energy due to the inability to equate the quantised momenta with the necessary points in $\underline{k}$-space. We thus need to find other extended eigenstates in the sea of edge states near the Dirac point to undertake a search in this set-up.

We mark sites using the triple-bond perturbation such as in Eq. (13). Throughout this section we choose the dimensions in terms of primitive cells of the graphene sheets, $(N_x, N_y) = (10, 10)$; a bearded edge sheet thus consists of $N = 200$ sites and a zigzag sheet is formed of $N = 218$ sites. The spectra of the search Hamiltonians for the bearded lattice is shown in Figure 14 constrained to the energy region of interest. The spectrum for zigzag edges is very similar and is not show here. One can clearly see an avoided crossing around the Dirac energy at $\gamma = 1$, the critical value for this type of perturbation. There are several states very close to the Dirac energy; these are the edge states which are all non-degenerate. Therefore, it is not possible for us to construct a superposition of degenerate eigenstates which is optimal for searching. Rather, our initial starting state must be a single eigenstates of the unperturbed Hamiltonian $\mathbf{H}_o = -\mathbf{A}$.

Using the search Hamiltonian from Eq. (13) and fixing $\gamma = 1$, we proceed by allowing the system to evolve after being prepared in one of the unperturbed eigenstates. One finds for both types of lattice, that the edge states near the Dirac energy fail to produce localisation behaviour; the probability at the neighboring vertices of the marked site do not rise above noise levels. Rather, search behaviour only begins to emerge when we use the first delocalised, non-edge state as our initial state. We also note that we *cannot* search for sites near the zigzag or bearded edges, where the edge states exist. Only as we move further into the bulk of the lattice or along an armchair-type edge, the localisation behaviour returns. Note that the edge states can be viewed as a kind-of one-dimensional system and, as we saw from the scaling argument towards the end of Sec. II, one-dimensional systems imply an energy spacing between successive energy levels of $E_{n+1} - E_n = \mathcal{O}\left(N^{-1}\right)$. Thus, the perturber state interacts with many states in a dense part of the spectrum and the search fails.

In Figure 15 we show the search behaviour arising from marked sites placed at different positions on a bearded graphene lattice (zigzag lattice types display similar behaviour). The results are similar to those found for the nanotube searches. There is a slight increase in variation of signal pattern with position, and an increase in success probability maxima as we move towards the centre of the lattice from either of the bearded edges.

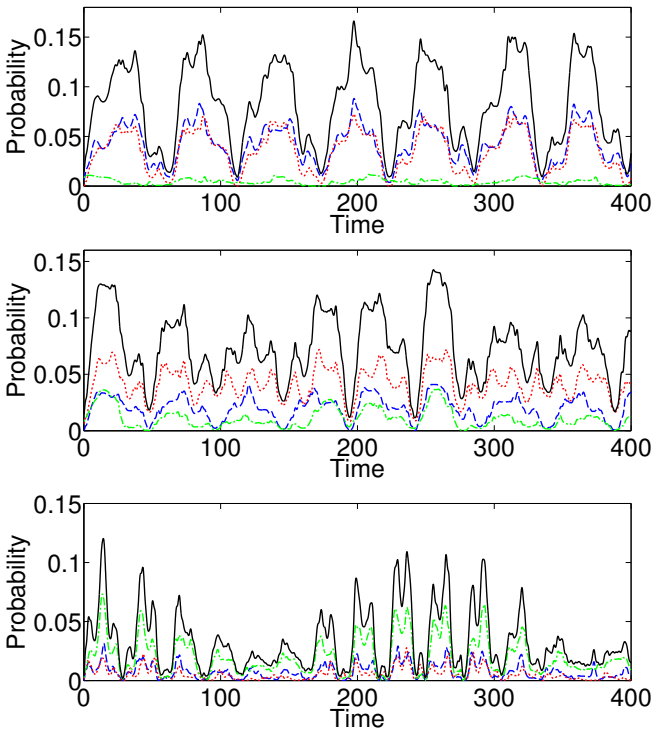


FIG. 15. (Color online) Searching on a bearded edge graphene sheet with dimensions $(N_x, N_y) = (10, 10)$ using the Hamiltonian, Eq. (13). All the searches are initialised in the first unperturbed, non-edge eigenstate above the Dirac energy. The locations of the marked vertices are: upper - halfway along the left armchair edge, middle - centre of the sheet, lower - at the mid-point of the lower bearded edge and a third of the way along the vertical axis. (Colors and linestyles as in Figure 12)

IX. DISCUSSION

We have shown that continuous-time quantum search can be done effectively on a two-dimensional graphene lattice without the use of internal degrees of freedom. This is achieved by making use of the conical (linear) dispersion relation in the graphene spectrum. The search succeeds in time $T = \mathcal{O}\left(\sqrt{N \ln N}\right)$ with probability $\mathcal{O}\left(1/\ln N\right)$. This is the same time complexity found in [3] for discrete-time searches and in [8] for continuous-time searches. To boost the probability to $\mathcal{O}\left(1\right)$, $\mathcal{O}\left(\ln N\right)$ repetitions are required giving a total time $T = \mathcal{O}\left(\sqrt{N} \ln^{\frac{3}{2}} N\right)$. Amplification methods [28–30] may be used to reduce the total search time further.

Our main result focusses on perturbations which involve altering the hopping potential from a marked site to all three of its nearest-neighbors equally. We have also demonstrated other types searches based on perturbing the hopping potential in a cell and the adding extra sites. We have shown that search mechanisms can be utilised for the purposes of signal transfer.

Our findings point towards applications in directed signal transfer, state reconstruction, or sensitive switching. This opens up the possibility of a completely new type of electronic engineering using single atoms as building blocks of electronic devices. Our results demonstrate that a range of nanostructures constructed from graphene could be used to this end.

ACKNOWLEDGMENTS

We thank Julian Böhm, Ulrich Kuhl and Fabrice Mortessagne for discussions on how the ideas of [10] could be adapted to more physical systems, which lead to some of the work on additional perturbation types and graphene flakes.

Appendix A: Calculation of $Z_2\left(S_{\underline{K}/\underline{K}'}, 1\right)$

We give here some details regarding the derivation of Eq. (35) and the logarithmic divergence of I_2. It is clear that the dominant contributions to the I_{2k} summations come from the vicinity of the Dirac points. Approximating the spectrum close to the Dirac points, one has

$$I_{2k} = 2\sqrt{3}N^{k-1}\left[\sum_{(p,q)\in L}\frac{1}{\left(S_{\underline{K},11}p^2 + 2S_{\underline{K},12}pq + S_{\underline{K},22}q^2\right)^k} + \sum_{(p,q)\in L}\frac{1}{\left(S_{\underline{K}',11}p^2 + 2S_{\underline{K}',12}pq + S_{\underline{K}',22}q^2\right)^k}\right] + O(1)\ . \tag{A1}$$

Here the sums over integers p and q is over a rectangular region L of the lattice $\mathbb{Z}^2$ which is centered at $(0,0)$ and has side lengths proportional to $\sqrt{N}$ – the center $(0,0)$, corresponding to the relevant Dirac point, is omitted from the sum. As stated in the main text, for $k > 1$ the corresponding sums converge which proves Eq. (34). For $k = 1$ we will establish constant C_1 and C_2 such that

$$C_1 \ln N < \sum_{(p,q)\in L}\frac{1}{S_{\underline{K},11}p^2 + 2S_{\underline{K},12}pq + S_{\underline{K},22}q^2} < C_2 \ln N \tag{A2}$$

which then directly leads to Eq. (35). To establish C_1 note that because each term in the sum (A2) is positive its value decreases by restricting it to a square region $-a_1\sqrt{N} \le p \le a_1\sqrt{N}$, $-a_1\sqrt{N} \le q \le a_1\sqrt{N}$ which is completely contained in L. Up to an error of order one the sum over a square region can in turn be written as a sum over eight terms of the form

$$\sum_{p=1}^{a_1\sqrt{N}}\sum_{q=1}^{p}\frac{1}{S_{\underline{K},11}p^2 \pm 2S_{\underline{K},12}pq + S_{\underline{K},22}q^2}\ . \tag{A3}$$

For fixed p we can find $q_{\max}$ such that

$$\sum_{q=1}^{p} \frac{1}{S_{\underline{K},11}p^2 \pm 2S_{\underline{K},12}pq + S_{\underline{K},22}q^2} > \frac{p}{S_{\underline{K},11}p^2 \pm 2S_{\underline{K},12}pq_{\max} + S_{\underline{K},22}q_{\max}^2} . \quad \text{(A4)}$$

We may choose $q_{\max} = b_1 p$ for some constant $b_1 \geq 0$, so

$$\sum_{p=1}^{a_1\sqrt{N}} \sum_{q=1}^{p} \frac{1}{S_{\underline{K},11}p^2 \pm 2S_{\underline{K},12}pq + S_{\underline{K},22}q^2} > c\sum_{p=1}^{\sqrt{N}} \frac{1}{p} \quad \text{(A5)}$$

which diverges as $\ln N$.

Establishing C_2 and the corresponding logarithmic bound from above, and thus proving Eq. (35), follows the same line by first extending the sum to a square of side length $2a_2\sqrt{N}$ that completely contains L and then establishing

$$\sum_{q=1}^{p} \frac{1}{S_{\underline{K},11}p^2 \pm 2S_{\underline{K},12}pq + S_{\underline{K},22}q^2} < \frac{p}{S_{\underline{K},11}p^2 \pm 2S_{\underline{K},12}pq_{\min} + S_{\underline{K},22}q_{\min}^2} \quad \text{(A6)}$$

with $q_{min} = b_2 p$.

[1] R. P. Feynman and A. R. Hibbs. *Quantum Mechanics and Path Integrals*, (McGraw-Hill Book Company, New York, NY, USA 1965), Chap. 2 *The Quantum-mechanical Law of Motion*.

[2] D. A. Meyer. From quantum cellular automata to quantum lattice gases, *Journal of Statistical Physics*, **85**(5 − 6):551-574, 1996.

[3] D. Aharonov, A. Ambainis, J. Kempe, and U. Vazirani. Quantum walks on graphs, In *Proceedings of the thirty-third annual ACM symposium on theory of computing*, (STOC '01, ACM, New York, NY, USA, 2001), pages 50-59.

[4] L. K. Grover. A fast quantum mechanical algorithm for database search, In *Proceedings of the twenty-eighth annual ACM symposium on theory of computing*, (STOC '96, ACM, New York, NY, USA, 1996), pages 212-219.

[5] L. K. Grover. Quantum mechanics helps in searching for a needle in a haystack, *Phys. Rev. Lett.*, **79**:325-328, 1997.

[6] N. Shenvi, J. Kempe, and K. B. Whaley. Quantum random-walk search algorithm, *Phys. Rev. A.*, **67**: 052307, 2003.

[7] A. Ambainis, J. Kempe, and A. Rivosh. Coins make quantum walks faster. In *Proceedings of the sixteenth annual ACM-SIAM symposium on discrete algorithms*, (Society for Industrial and Applied Mathematics, Philadelphia, PA, USA, 2005), pages 1099-1108.

[8] A. M. Childs and J. Goldstone. Spatial search by quantum walk, *Phys. Rev. A*, **70**:022314, 2004.

[9] A. M. Childs and J. Goldstone. Spatial search and the Dirac equation, *Phys. Rev. A*, **70**:042312, 2004.

[10] I. Foulger, S. Gnutzmann, and G. Tanner. Quantum search on graphene lattices, *Phys. Rev. Lett.*, **112**: 070504, 2014.

[11] A. M. Childs and Y. Ge. Spatial search by continuous-time quantum walks on crystal lattices, *Phys. Rev. A.*, **89**:052337, 2014.

[12] J. Boehm, M. Bellec, F. Mortessagne, U. Kuhl, S. Barkhofen, S. Gehler, H.J. Stöckmann, I. Foulger, S. Gnutzmann, and G. Tanner. Experiments on 'quantum' search and directed transport in microwave artificial graphene, *Phys. Rev. Lett.*, **114**:110501, 2015.

[13] G. Abal, R. Donangelo, F. I. Marquezino, and R. Portugal, Spatial search on a honeycomb network, *Math. Structures in Comp. Sci.*, **20** 999, 2010.

[14] E. Farhi and S. Gutmann. Quantum computation and decision trees, *Phys. Rev. A*, **58**:915-928, 1988.

[15] C. Kittel, *Introduction to Solid State Physics*, (John Wiley & Sons, Hoboken, NJ, USA, 8th ed., 2004), Chap. 9 *Fermi Surfaces and Metals*.

[16] B. Hein and G. Tanner. Quantum search algorithms on the hypercube, *J. Phys. A: Math. Theor.*, **42**:085303, 2009.

[17] B. Hein and G. Tanner. Wave communication across regular lattices, *Phys. Rev. Lett.*, **103**:260501, 2009.

[18] P. R. Wallace. The Band Theory of Graphite, *Phys. Rev.*, **71**:622, 1947.

[19] Castro Neto, A. H. and Guinea, F. and Peres, N. M. R. and Novoselov, K. S. and Geim, A. K., The electronic properties of graphene, *Rev. Mod. Phys.*, **81**:109, 2009.

[20] H.-S. P. Wong and D. Akinwande. *Carbon Nanotube and Graphene Device Physics*, (Cambridge University Press, Cambridge, UK, 2011), Chap. 3 *Graphene*.

[21] C.L. Siegel. *On Advanced Analytic Number Theory*, (Tata Institute of Fundamental Research, Mumbai, India, 1961), Chap. 1 *Kronecker's Limit Formulas*.

[22] J.C. Meyer *et al.* Direct Imaging of Lattice Atoms and Topological Defects in Graphene Membranes, *Nano Lett.*, **8**:3582, 2008.

[23] F. Banhart, J. Kotakoski, and A. V. Krasheninnikov. Structural Defects in Graphene, *ACS Nano*, **5**(1): 26-41, 2011.

[24] H.-S. P. Wong and D. Akinwande. *Carbon Nanotube and Graphene Device Physics*, (Cambridge University Press, Cambridge, UK, 2011), Chap. 4 *Carbon Nanotubes*.

[25] K. Wakabayashi, K. Sasaki, T. Nakanishi, and T. Enoki. Electronic states of graphene nanoribbons and analytical solutions, *Science and Technology of Advanced Materials*, **5**(1):054504, 2010.

[26] W. Yao, S. A. Yang, and Q. Niu. Edge states in graphene: From gapped flat-band to gapless chiral modes, *Phys. Rev. Lett.*, **102**(9):096801, 2009.

[27] A. Ambainis, A. Bačkurs, N. Nahimovs, R. Ozols and A. Rivosh. Search by Quantum Walks on Two-Dimensional Grid without Amplitude Amplification. In *Theory of Quantum Computation, Communication, and Cryptography*, (Springer Berlin Heidelberg, Berlin, Germany,

2013), pages 87-97.

[28] L. K. Grover, Quantum Computers Can Search Rapidly by Using Almost Any Transformation *Phys. Rev. Lett.*, **80**:4329, 1998.

[29] A. Tulsi, Faster quantum-walk algorithm for the two-dimensional spatial search, *Phys. Rev. A*, **78**:012310, 2008.

[30] V. Potoček, A. Gábris, T. Kiss, and I. Jex, Optimized quantum random-walk search algorithms on the hypercube, *Phys. Rev. A*, **79**:012325, 2009.